Long-range electron transport in Prussian blue analog nanocrystals.

Roméo Bonnet[1,*], Stéphane Lenfant[1], Sandra Mazérat[2],
Talal Mallah[2,#] and Dominique Vuillaume[1,#]

1. Institute for Electronics Microelectronics and Nanotechnology (IEMN), CNRS, Av. Poincaré, 59652 Villeneuve d'Ascq, France.

2. Institut de Chimie Moléculaire et des Matériaux d'Orsay (ICMMO), CNRS, University Paris-Sud, Rue du doyen Georges Poitou, 91405 Orsay, France.

* Now at: ITODYS, CNRS, Univ. Paris-Diderot, 15, rue Jean Antoine de Baïf, 75013 Paris, France.

Corresponding authors : talal.mallah@u-psud.fr; dominique.vuillaume@iemn.fr

SUPPORTING INFORMATION

1. Preparation and characterization of the $CsNiCr(CN)_6$ (abbreviated as CsNiCr) and $CsCoFe(CN)_6$ (abbreviated as CsCoFe) nanocrystals

CsNiCr nanocrystals.

1 - The nanocrystals were prepared as in ref. 1: an aqueous solution (100 mL) containing $NiCl_2.6H_2O$ (0.2×10^{-3} mol, $c = 2 \times 10^{-3}$ M) and CsCl (0.4×10^{-3} mol, $c = 4 \times 10^{-3}$ M) was added rapidly in an equal volume of an aqueous solution of $K_3[Cr(CN)_6]$ (0.2×10^{-3} mol, $c = 2 \times 10^{-3}$ M) under vigorous stirring. The solution was stirred for one hour.

2 - Dynamic light scattering (DLS) of the as-prepared solution was measured and shows a hydrodynamic diameter of 6 nm (Figure S1). The zeta potential measured was found to be equal to -31 mV indicating the presence of negatively charged particles in the solution.

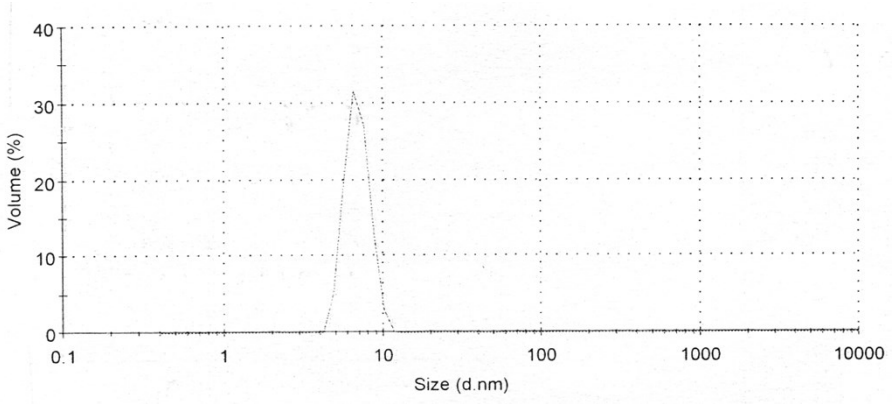

Figure S1. DLS of the as-prepared colloidal solution of CsNiCr nanocrystals.

3 - Transmission Electron Microscopy (TEM) imaging of the as-prepared nanocrystals show cubic objects with a size close to 6 nm confirming the DLS data. It is worth noting that the objects are not very stable under the electron beam making difficult to focus on small areas. TEM images were acquired on different areas of the grid giving the same results (Figure S2).

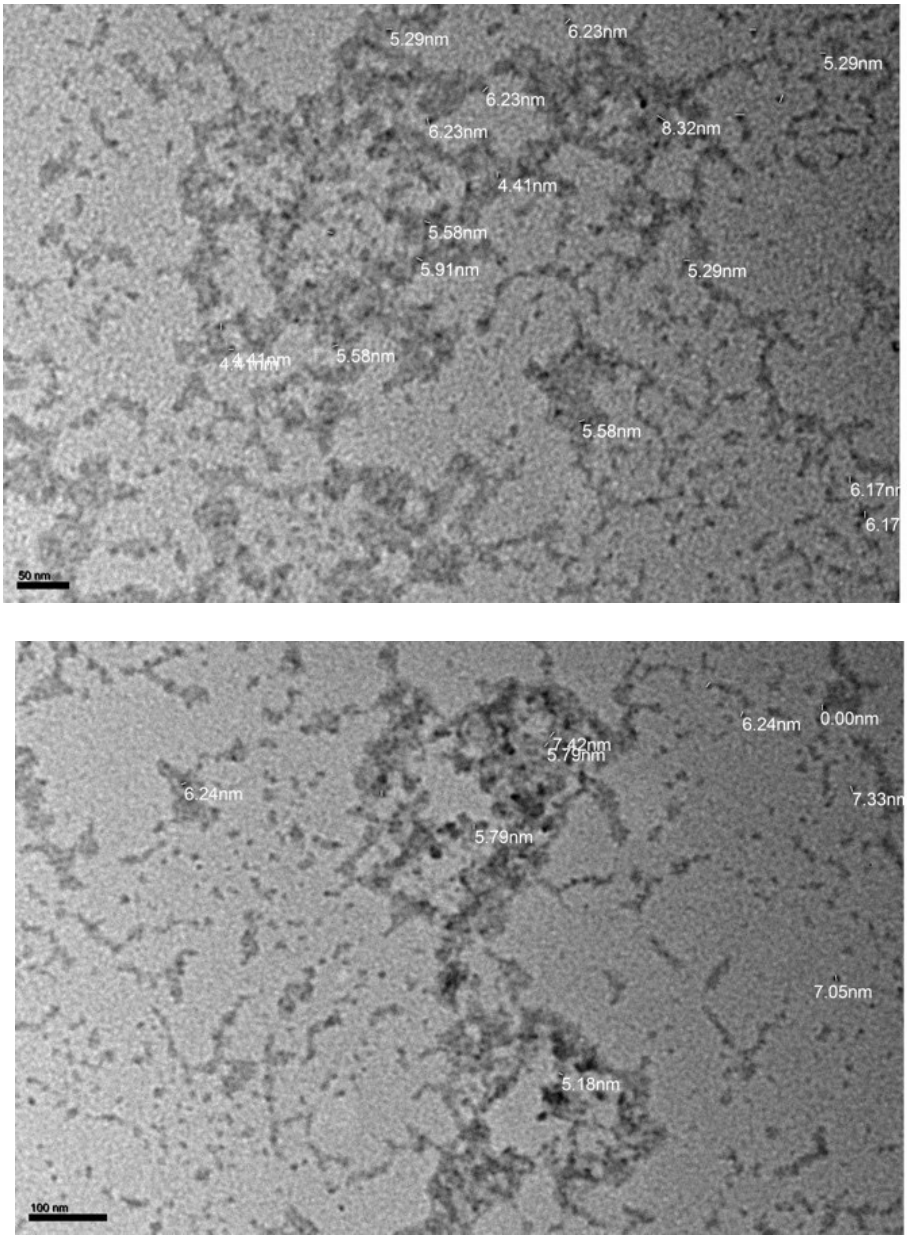

Figure S2. Transmission Electron Microscopy imaging of the CsNiCr nanocrystals on two different regions of the grid.

4 - Infra-red spectroscopy of the nanocrystals was performed on a solid material obtained by recovering the objects after adding excess methanol on the colloidal solution. The spectrum (Figure S3) show in the 2200-2000 cm^{-1} region the asymmetric vibration mode of the cyanide at 2171 cm^{-1} characteristics of cyanide bridging a trivalent metal ion (Cr(III) here) and a divalent one (Ni(II) here) corresponding to the Cr-CN-Ni sequence as expected.[1] The shoulder at 2134 cm^{-1} is assigned to

non-bridged cyanides coordinated to Cr(III) as expected for $Cr(CN)_6$ species present at the surface of the nanocrystals.

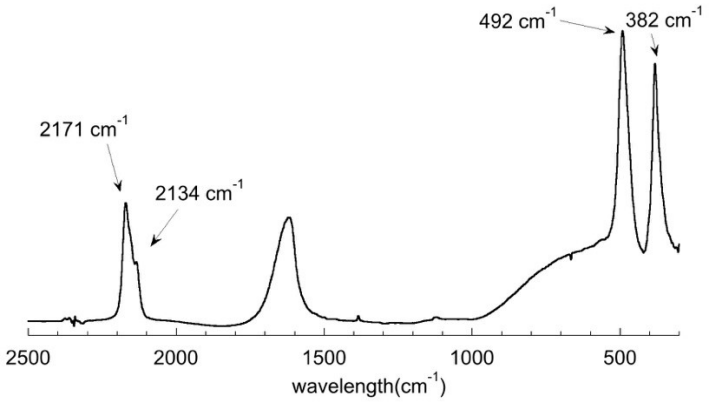

Figure S3. Infra-red spectrum of CsNiCr nanocrystals, the band at 1630 cm^{-1} corresponds to water molecules.

5 - X-ray diffraction on a powder sample obtained by recovering the nanocrystals by addition of an excess of CTABr (Cetyltrimethylammonium bromide) show a pattern (Figure S4) corresponding to a face centered cubic structure with a cell parameter a = 10.50 Å as expected.[1] The size of the crystalline domains determined using the Scherrer equation was found equal to 6.2 nm confirming the DLS and TEM data.

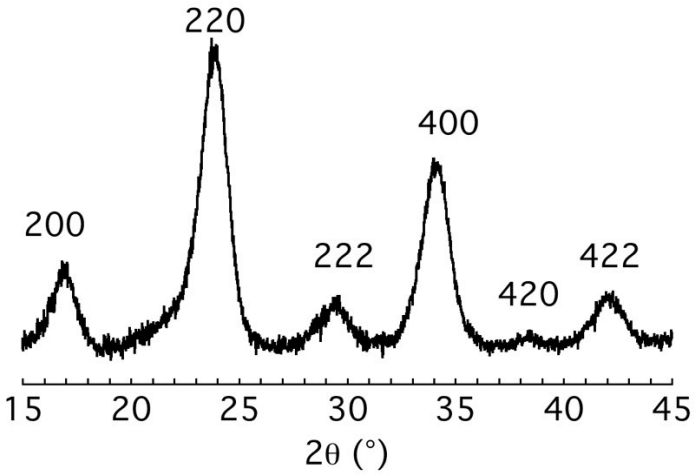

Figure S4. Powder X-ray diffraction pattern of the CsNiCr nanocrystals.

6 - Energy dispersive X-ray Spectroscopy carried of the as-prepared nanocrystals casted on a grid give the following atomic percentages Cs (33.17%), Ni (34.36%) and Cr (32.46%) corresponding to the following formula: $Cs_{0.96}Ni[Cr(CN)_6]_{0.94}$.

CsFeCo nanocrystals.

1 - The $CsFeCo(CN)_6$ nanocrystals were prepared using the same procedure as for the $CsNiCr(CN)_6$ ones replacing Ni(II) and Co(II) and Cr(III) by Fe(III).

2 - Dynamic light scattering (DLS) of the as prepared colloidal solution (Figure S5) show the presence of objects with hydrodynamic diameter of 15 nm.

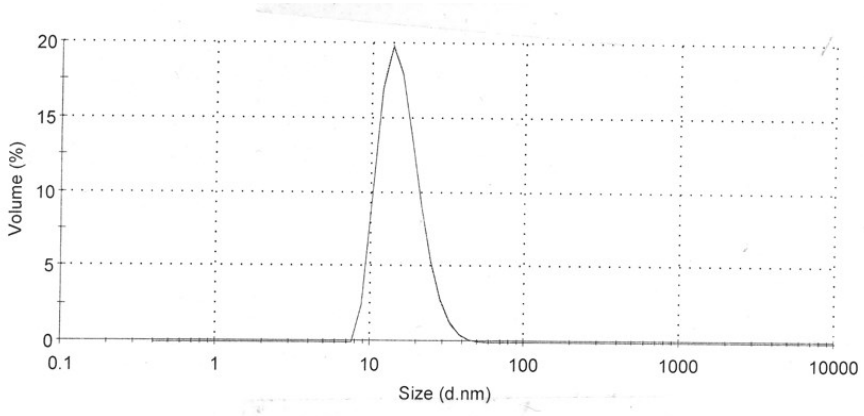

Figure S5. DLS of the as-prepared colloidal solution of CsCoFe nanocrystals.

3 - Transmission Electron Microscopy (TEM) imaging of the as-prepared nanocrystals show cubic objects with a size close to 15 nm confirming the DLS data.

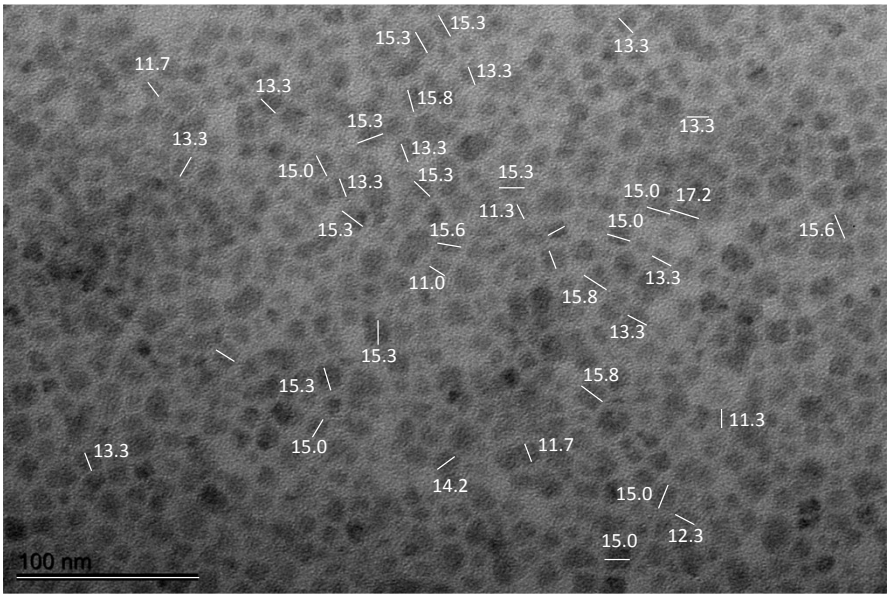

Figure S6. Transmission Electron Microscopy imaging of the CsCoFe nanocrystals.

4 - Infra-red spectroscopy of the nanocrystals was performed on a solid material obtained by recovering the objects after precipitating the colloidal solution with $CaCl_2$. The spectrum (Figure S7) show in the 2200-2000 cm^{-1} region the asymmetric vibration mode of the cyanide at 2120 cm^{-1} characteristics of cyanide bridge corresponding to the Fe(II)-CN-Co(III) sequence as expected for a when an electron transfer occurs during the reaction between $Fe^{III}(CN)_6^{3-}$ and $Co^{II}(H_2O)_6^{2+}$.[2]

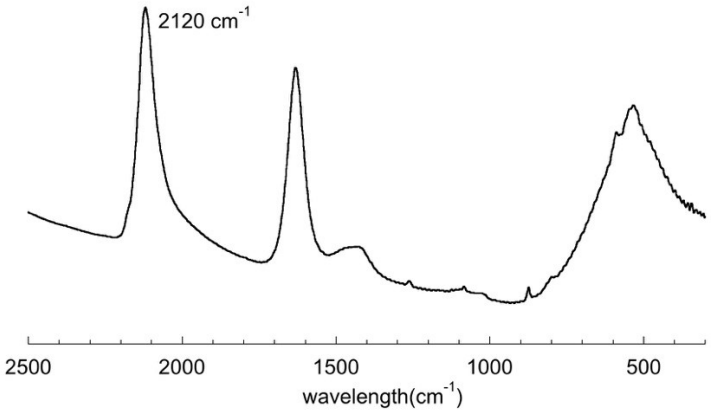

Figure S7. Infra-red spectrum of CsCoFe nanocrystals, the band at 1630 cm^{-1} corresponds to water molecules.

5 - X-ray diffraction on a powder sample obtained by recovering the nanocrystals by addition of an excess of CTABr (Cetyltrimethylammonium bromide) show a pattern (Figure S8) corresponding to a face centered cubic structure with a cell parameter a = 10.02 Å as expected for the presence of a majority of Fe^{II}-CN-Co^{III} pairs within the nanocrystals.[3] The size of the crystalline domains determined using the Scherrer equation was found equal to around 11 nm.

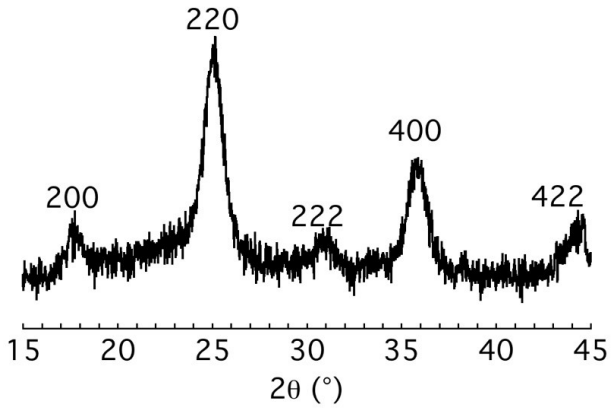

Figure S8. Powder X-ray diffraction of the CsFeCo nanocrystals.

6 - Energy dispersive X-ray Spectroscopy carried of the nanocrystals recovered by addition of an excess of CTABr (Cetyltrimethylammonium bromide), redispersed in methanol and casted on a grid give the following atomic percentages Cs (27.61%), Co (38.7%) and Fe (33.7%) corresponding to the following formula: $Cs_{0.7}Co[Fe(CN)_6]_{0.9}$. This formula does not include the CTA^+ that acts as counter-

anions for the negatively charged nanocrystals, the Cs^+ ions are present within the tetrahedral sites of the fcc nanocrystals.

2. Additional AFM images and histograms of heights.

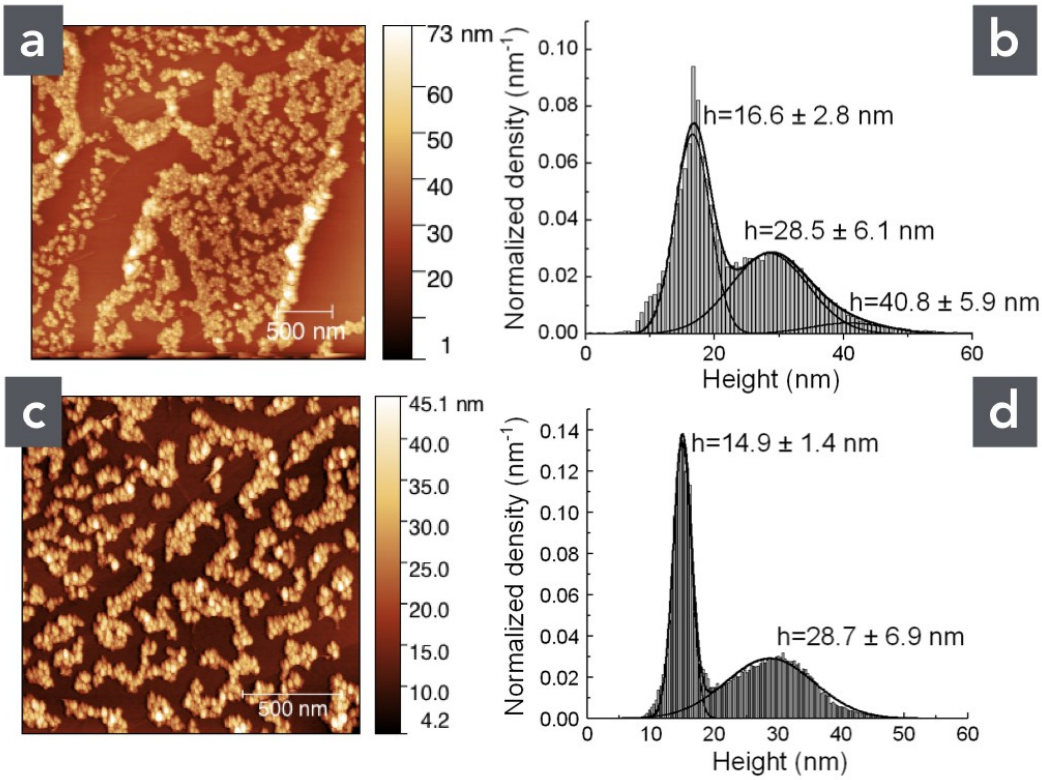

Figure S9. (a, c) Topographic AFM image and corresponding histograms of heights **(b, d)** of the CsCoFe layers. Fig. S9-a is a zoom of the Figure 1-c in the main text. Fig. S9-c is taken on another zone of the sample. In panels (b) and (d), the values marked for each peaks are the average heights and the standard deviations obtained from the fits of multi-Gaussian distributions (black lines).

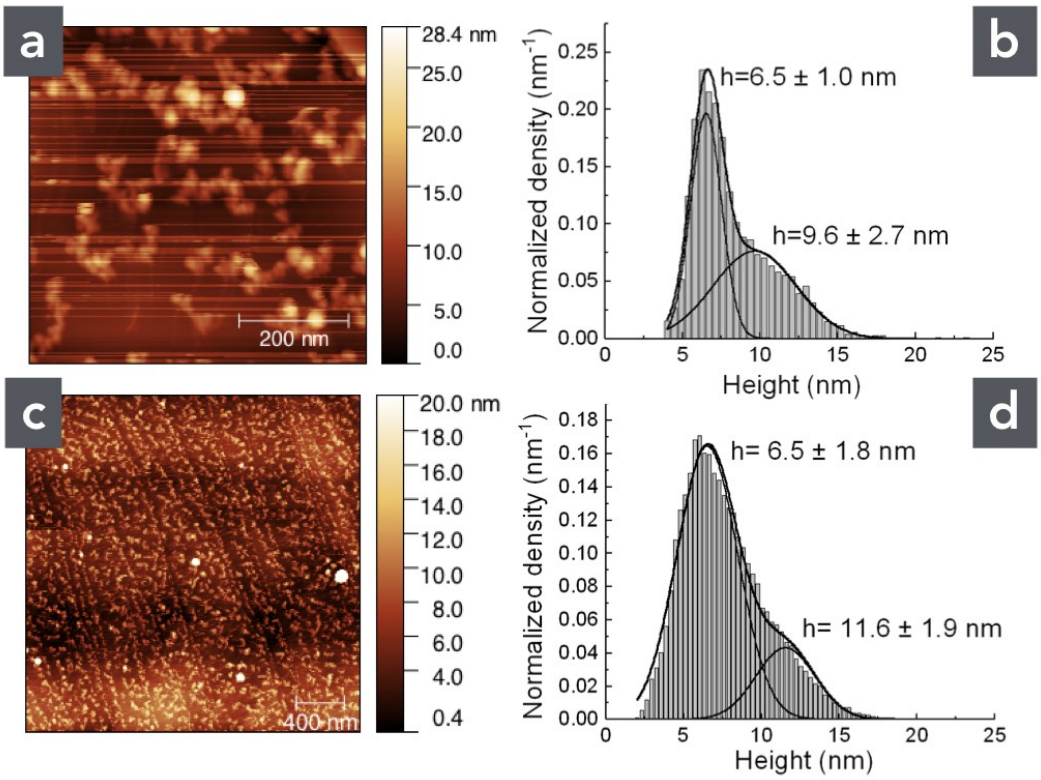

Figure S10. (a, c) Topographic AFM image and corresponding histograms of heights **(b, d)** of the CsNiCr layers taken on two other zones of the sample. In panels (b) and (d), the values marked for each peaks are the average heights and the standard deviations obtained from the fits of multi-Gaussian distributions (black lines). In (a, b) the horizontal defects/lines (image instabilities) have been masked for the histogram analysis.

3. Analysis of the particle size on surfaces (AFM and SEM images).

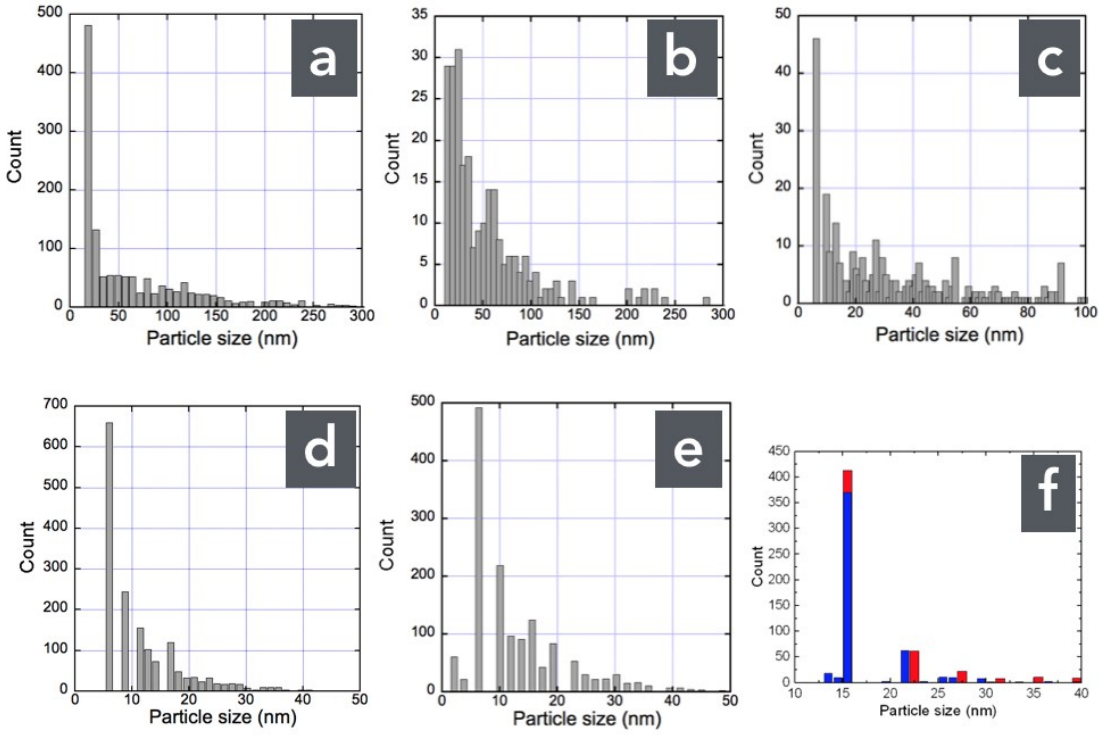

Figure S11. (a,b,c) CsCoFe : histograms of the particle sizes calculated from the AFM images Figs. 1-c, S9-a and S9-c, respectively. **(d,e)** CsNiCr : histograms of the particle sizes calculated from the AFM images Figs. 1-e and S10-c, respectively. The thresholding method was used for the grain analysis, and, assuming a square face of the PBA, the plotted particle size is the square root of the calculated projected (flat) area of the grain. **(f)** CsCoFe : histograms of the particle sizes calculated from the SEM images Figs. 1-a (in red) and Fig. 1-b (in blue).

4. Histograms of the tip z-position during the C-AFM measurements.

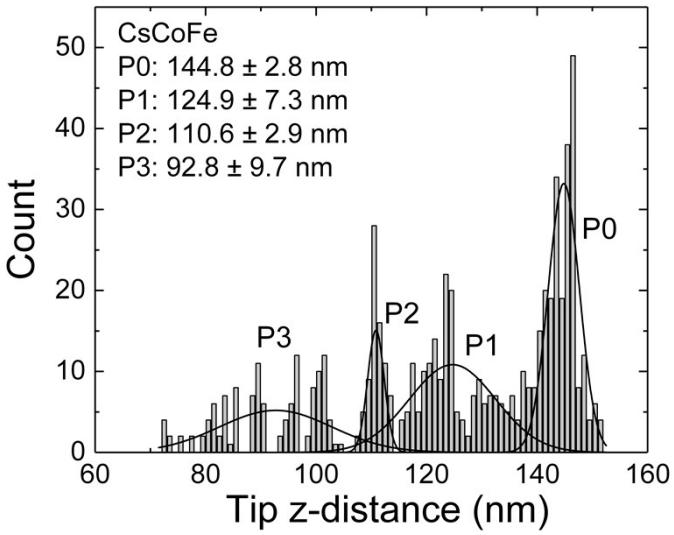

Figure S12. CsCoFe. Histograms of the tip z-position (0 = tip retracted). The z-position is recorded simultaneously for each I-V curve (500 I-V traces). The mean value and standard deviation (Gaussian fits) are given in the figure for each peaks.

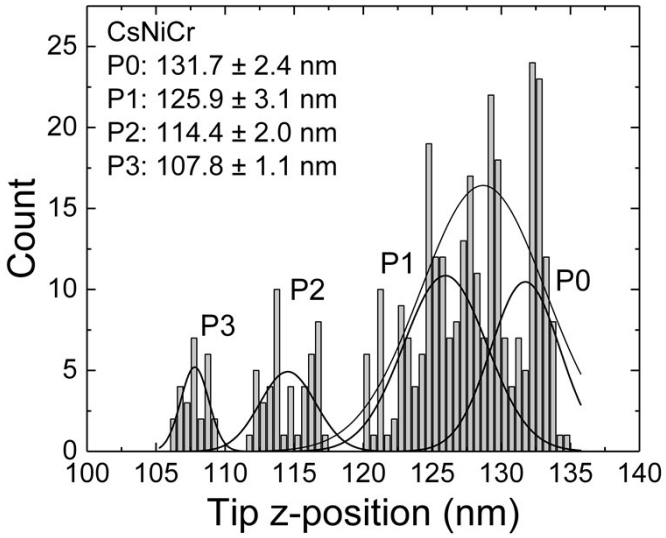

Figure S13. CsNiCr. Histograms of the tip z-position (0 = tip retracted). The z-position is recorded simultaneously for each I-V curve (500 I-V traces). The mean value and standard deviation (Gaussian fits) are given in the figure for each peaks. The large peak (thin line) can be decomposed into 2 contributions (P0 and P1).

5. Current-voltage measurements on the bare HOPG substrates.

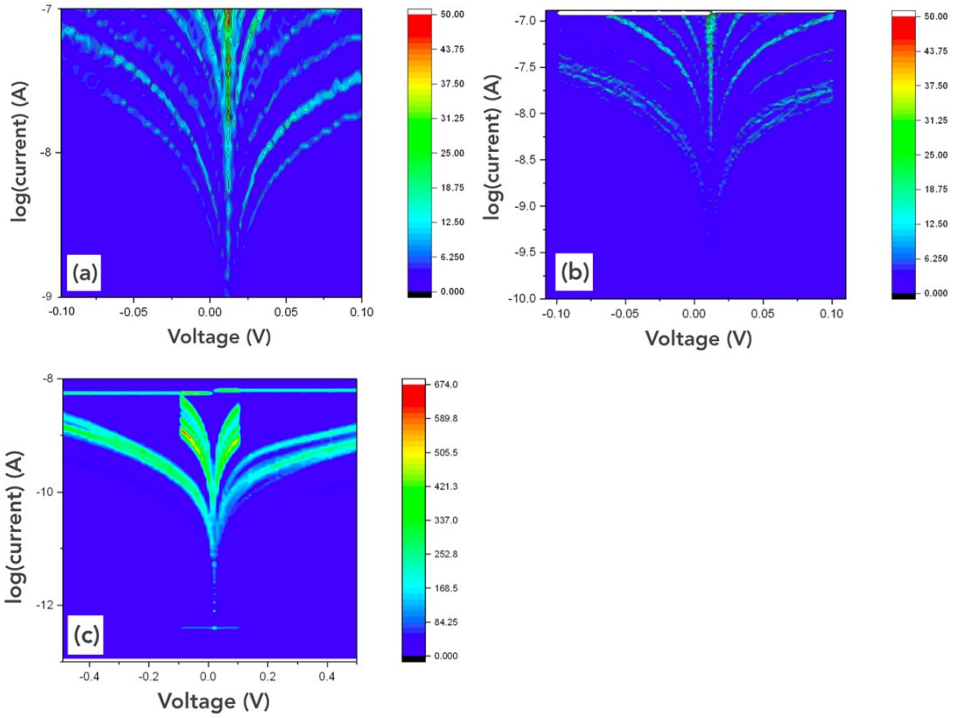

Figure S14. (a and b) Typical I-V 2D histograms of the bare HOPG substrates used for the deposition of CsCoFe (2 zones). The I-V curves correspond to peak P0 in Fig. 2-a (currents above 10 nA at low voltages ±0.1 V). **(c)** Typical I-V 2D histograms of the bare HOPG substrates used for the deposition of CsNiCr showing three zones (currents above current preamp saturation - horizontal line, currents between 1 and 10 nA at ±0.1V and a zone less conducting with currents around nA at ± 0.5 V corresponding to peak P0 in Fig. 3-a. All currents plotted on decimal log scales.

6. Topographic AFM and conducting AFM on thick films.

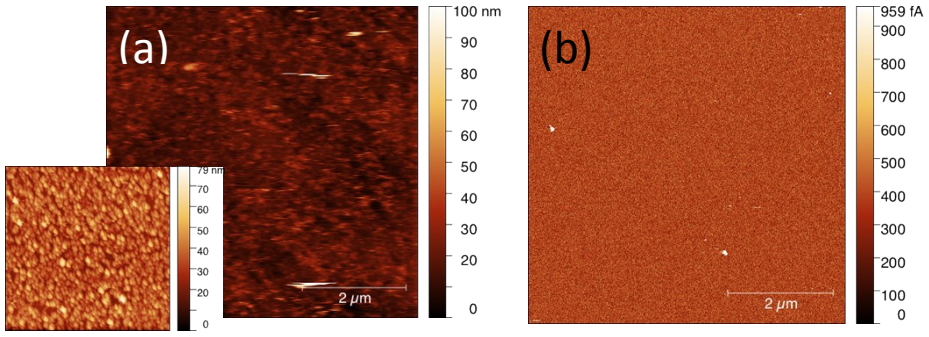

Figure S15. (a) Topographic AFM image of a thicker CsCoFe film with a complete coverage of the HOPG substrate (inset: zoom on a 2 µm x 2 µm zone), and **(b)** corresponding conducting-AFM (at 50 mV) showing no current (below the sensitivity limit of about 5×10^{-13} A).

7. Detailed statistical analysis of the decay factor β.

For each I-V curve in the data sets of Figs. 2 and 3, we plot the current measured at 50, 200 and 400 mV versus the tip height relative to the surface. This value is deduced from the z-position, z, which is recorded simultaneously for each I-V traces (Figs. S12 and S13) and the height, h, relative to the surface, PBA layer thickness, is calculated by h = -(z - z(P0)), where z(P0) is the average z value for the peak P0 determined in the histograms in Figs. S12 and S13. We discard from this analysis the I-V traces that are too noisy (especially for low current below 10^{-12} A) or exhibit a too large hysteresis during the back and forth voltage sweep or abrupt "staircase-like" jumps in the current, which may indicate instabilities of the C-AFM tip contact on the samples. The resulting data (Fig. S16) are fitted by a linear regression to deduce the decay factor β indicated on the plots.

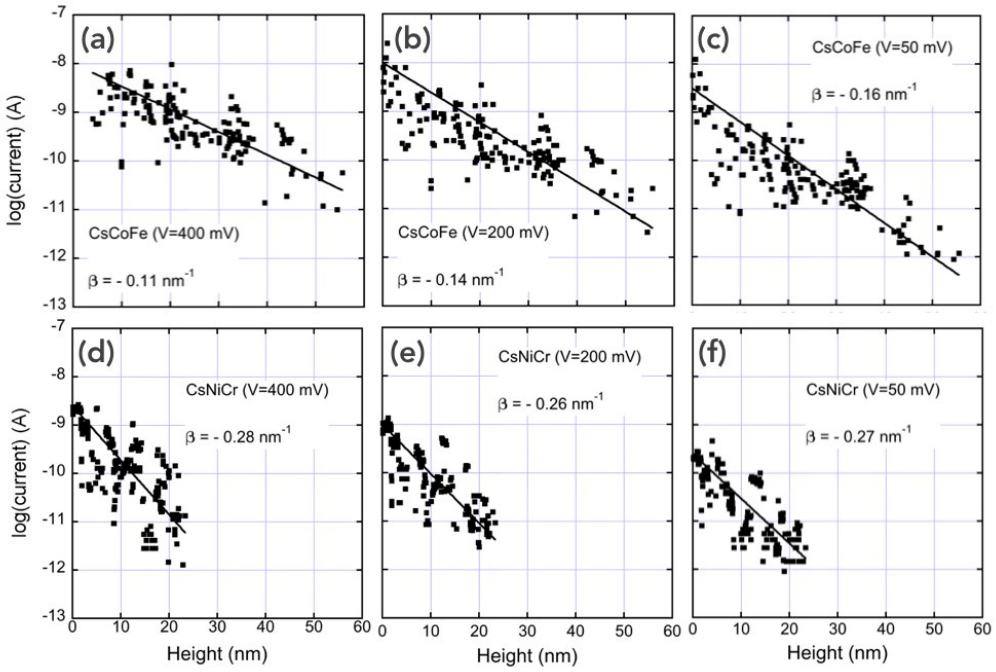

Figure S16. Decimal log of current (at V=400, 200 and 50 mV) versus PBA layer height for the CsCoFe, 354 I-V traces **(a-c)** and CsNiCr, 368 I-V traves **(d-e)** samples.

8. Additional fits of the single molecular energy level model on peak P1.

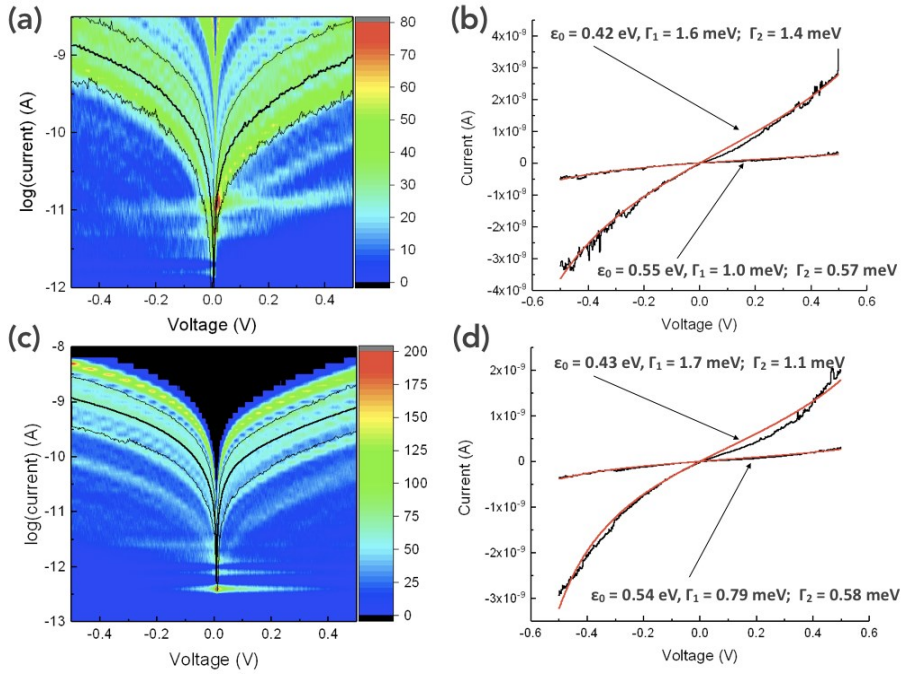

Figure S17. (a) CsCoFe. The thin black lines are the IV curves bounding the Gaussian distribution of peak P1 (the bold black line is the average IV, see Fig. 2-a). **(b)** Fits (red lines) of the single molecular energy level model (Eq. 1, main texte) on the two lower and upper limit current voltage curves (black lines) shown in Fig. S2-a. The fitted parameters are given on each figures. **(c and d)** Same as (a and b) for peak P1 of CsNiCr. (panels a and c, currents plotted on decimal log scale).

9. Detailed statistical analysis of the energy levels.

Following the same protocol as for Figs. S16, we fit the single energy level model (Eq. 1 in main text) on each I-V traces from the sets of data of the CsCoFe and CsNiCr samples. We discard the I-V traces that are too noisy (especially for low current below 10^{-12} A) or exhibit a too large hysteresis during the back and forth voltage sweep or abrupt "staircase-like" jump in the current, since the fits are not accurate enough or significant in such cases. Figs. S18-a and S19-a show the ε_0 values versus height (as determined above, section 7) for the CsCoFe and CsNiCr samples, respectively. Figs. S18-c and S19-c show the histograms of the ε_0 values and the Gaussian fits. In both figure, the panels "b" plot the histograms of heights. The dashed lines are simulated Gaussian curves with the height parameters (mean values and standard deviations) directly determined from the topographic (TM-AFM) images shown in Fig. 1 (main text). Albeit the determination of the heights used for these statistical analyses (also for Figs. S16) is indirect and likely less accurate than a direct height measurement as in the topographic TM-AFM, the agreement is satisfactory. We also observe peaks corresponding of the configurations with one (P1), two (P2) and three (P3) PBA nanocrystals in the

HOPG/PBAs/C-AFL tip nanodevices. We just note a weak shift of the peak maxima between the two approaches (about 2 nm), which remains reasonable given the weaker accuracy of the indirect height determination.

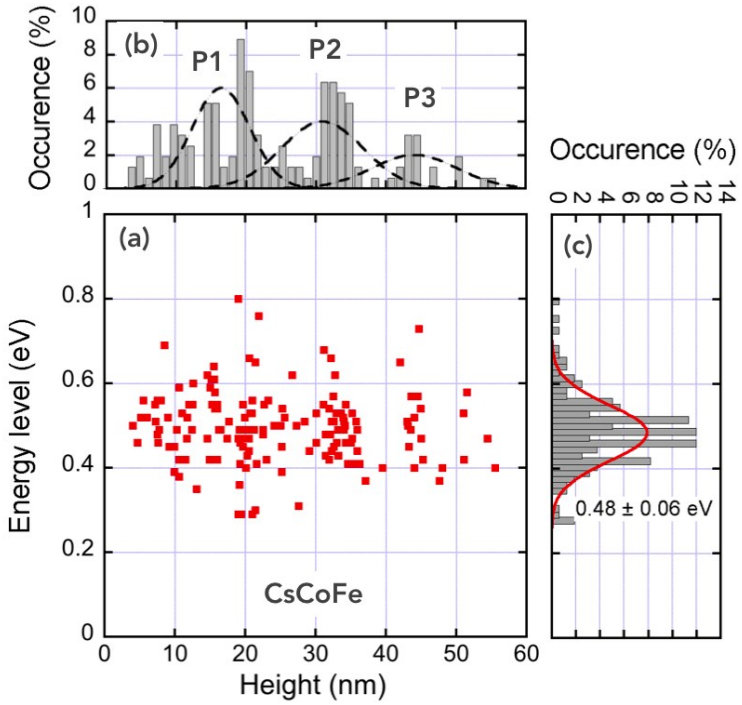

Figure S18. CsCoFe. **(a)** Statistical determination of the energy value ε_0 (from 354 I-V traces), and corresponding **(b)** histogram of heights and **(c)** histograms of energy values. The red line is a Gaussian fit given ε_0 = 0.48 ± 0.06 eV.

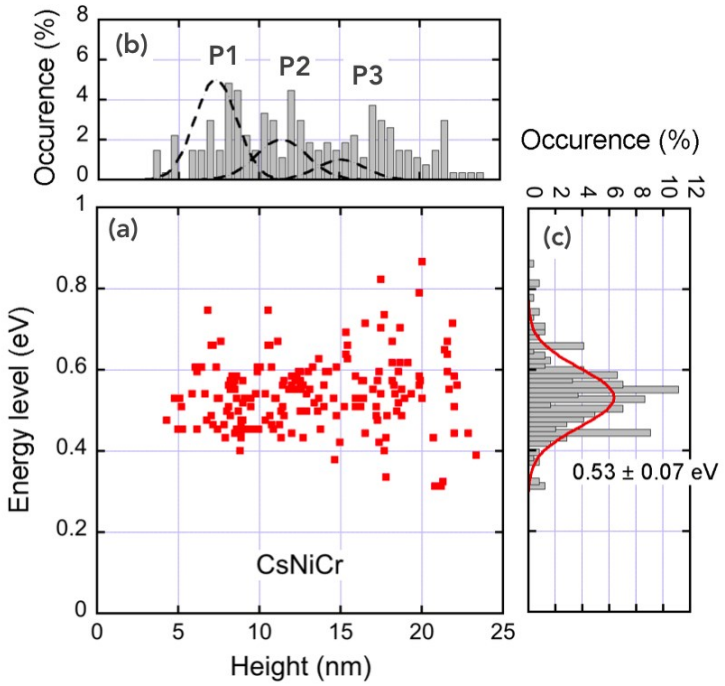

Figure S19. CsNiCr. **(a)** Statistical determination of the energy value ε_0 (from 368 I-V traces), and corresponding **(b)** histogram of heights and **(c)** histograms of energy values. The red line is a Gaussian fit given $\varepsilon_0 = 0.53 \pm 0.07$ eV.

10. Conductance versus 1/distance and electric field.

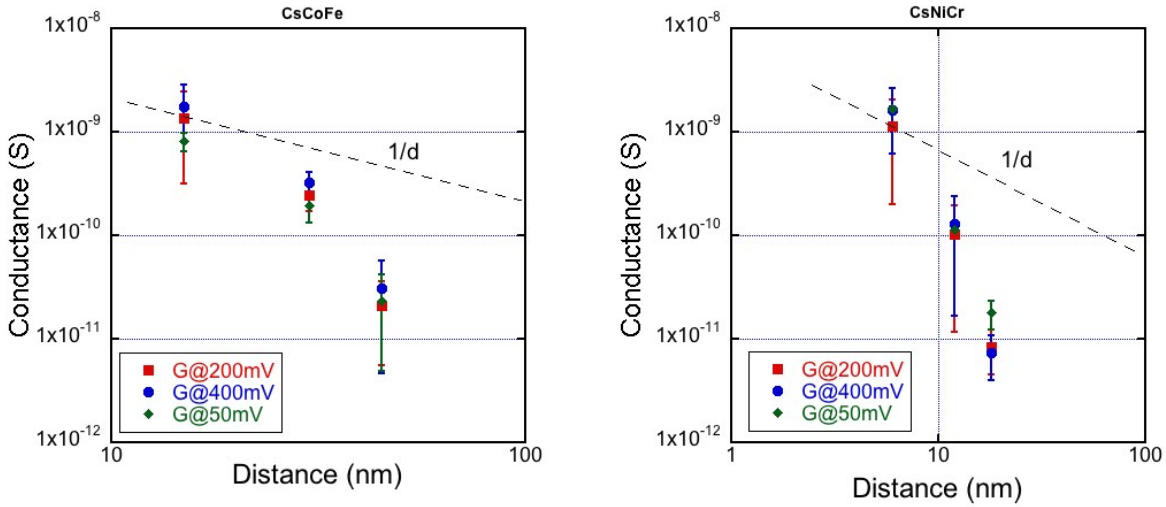

Figure S20. Conductance (calculated from the average current peaks P1,P2 and P3 divided by the applied voltage : blue points at 400 mV, red points at 200 mV, green points at 50 mV) vs. 1/d (log-log scale, expected 1/d behavior shown by dashed lines with a slope -1).

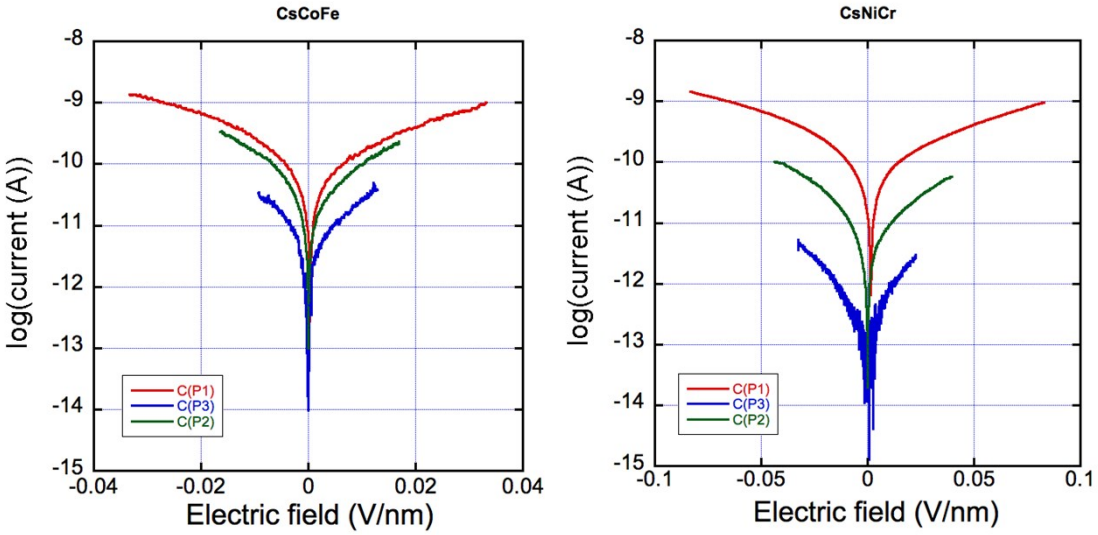

Figure S21. Average I-V for the 3 peaks (P1 in red, P2 in green, P3 in blue, all currents plotted on decimal log scales) vs. electric field. They are not superimposed as it should be for a field-driven hopping mechanism.[4, 5]

11. Fits of the single molecular energy level model on peaks P2 and P3.

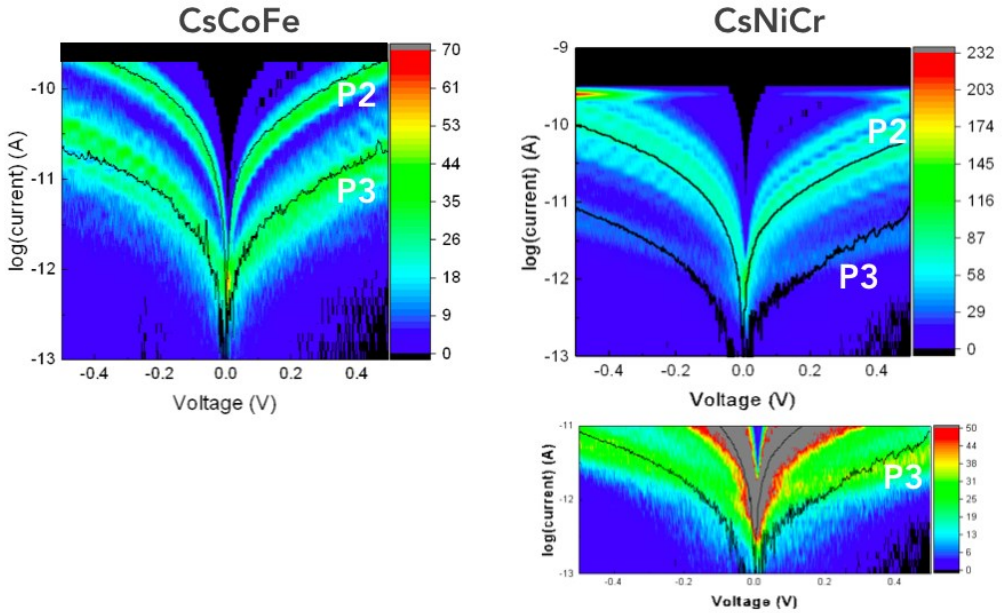

Figure S22. Average I-V curves (all currents plotted on decimal log scales) for the peaks P2 and P3 (218 I-V traces for P2 CsCoFe; 123 I-V traces for P3 CsCoFe; 353 I-V traces for P2 CsNiCr). Note that the average I-V for the CsNiCr peak P3 is not very accurate since data are very noisy at this low level

of current and we have only a small number of I-V traces (<50) for this peak (lower right graph is a zoom on P3).

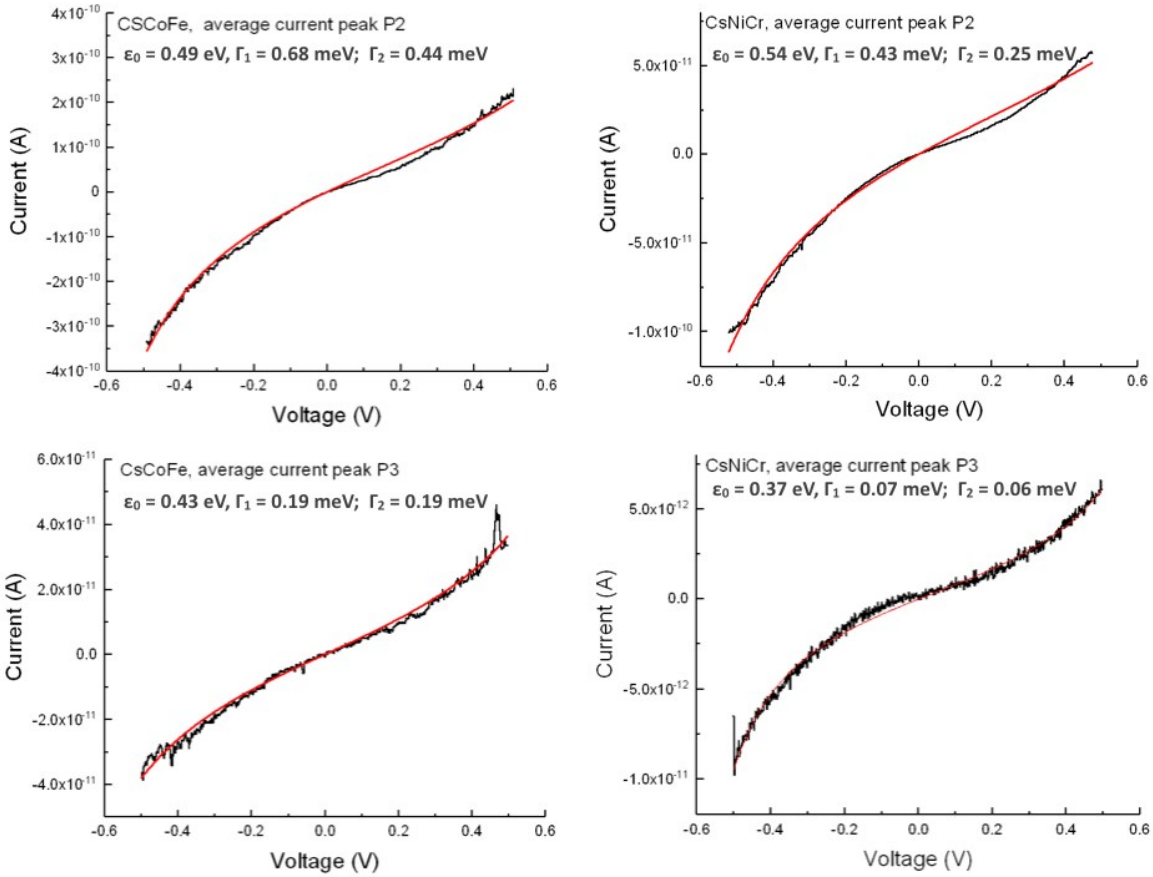

Figure S23. Fits (red lines) of the single molecular energy level model (Eq. 1, main texte) on the average current voltage curves (black lines) for the peaks P2 and P3. The fitted parameters are given on each figures. We note a decrease of the ε_0 value for the CsNiCr peak P3 (with respect of the values for P1 and P2), which may be due to the inaccurate determination of the average I-V (see figure S19).

References

1. D. Brinzei, L. Catala, N. Louvain, G. Rogez, O. Stephan, A. Gloter and T. Mallah, *Journal of Materials Chemistry*, 2006, **16**, 2593-2599.
2. A. C. Felts, M. J. Andrus, C. M. Averback, C. H. Li and D. R. Talham, *Polyhedron*, 2017, **133**, 404-411.

3. A. Bleuzen, C. Lomenech, V. Escax, F. Villain, F. Varret, C. C. D. Moulin and M. Verdaguer, *J Am Chem Soc*, 2000, **122**, 6648-6652.
4. S. H. Choi, B. Kim and C. D. Frisbie, *Science*, 2008, **320**, 1482-1486.
5. S. H. Choi, C. Risko, M. C. R. Delgado, B. Kim, J.-L. Brédas and C. D. Frisbie, *J Am Chem Soc*, 2010, **132**, 4358-4368.